AIAA-97-2475

Overview of X-38 Hypersonic Aerothermodynamic Wind Tunnel Data and Comparison with Numerical Results

C. Campbell and J. Caram
NASA Johnson Space Center
Houston, TX 77058

S. Berry, T. Horvath, and N. Merski
NASA Langley Research Center
Hampton, VA 23681

M. Loomis
NASA Ames Research Center
Moffett Field, CA 94035

E. Venkatapathy
Thermosciences Institute
Moffett Field, CA 94035

32nd AIAA Thermophysics Conference

June 23-25, 1997 / Atlanta, GA

An Overview of X-38 Hypersonic Aerothermodynamic Wind Tunnel Data and Comparison with Numerical Results

Charles H. Campbell*
Jose M. Caram*
NASA Johnson Space Center Houston, TX 77058

Scott A. Berry,¶ Thomas J. Horvath,¶ N. Ronald Merski¶
NASA Langley Research Center Hampton, VA 23681

Mark P. Loomis§
NASA Ames Research Center, Moffett Field, CA 94035

Ethiraj Venkatapathy‡
Thermosciences Institute, Moffett Field CA 94035

Abstract

A NASA team of engineers has been organized to design a crew return vehicle for returning International Space Station crew members from orbit. The hypersonic aerothermodynamic characteristics of the X-23/X-24A derived X-38 crew return vehicle are being evaluated in various wind tunnels in support of this effort. Aerothermodynamic data from two NASA hypersonic tunnels at Mach 6 and Mach 10 has been obtained with cast ceramic models and a thermographic phosphorus digital imaging system. General windward surface heating features are described based on experimental surface heating images and surface oil flow patterns for the nominal hypersonic aerodynamic orientation. Body flap reattachment heating levels are examined. Computational Fluid Dynamics tools have been applied at the appropriate wind tunnel conditions to make comparisons with this data.

Nomenclature

b	=	reference span, in.
c	=	reference chord, in.
L	=	X-38 reference length, in.
L_x	=	axial reference length, in.
L_y	=	spanwise reference length, in.
S_{ref}	=	reference area, in^2
X	=	X (axial) vehicle coordinate, in.
Y	=	Y (lateral) vehicle coordinate, in.
Z	=	Z (vertical) vehicle coordinate, in.
M_∞	=	freestream Mach number
P_{t1}	=	stagnation pressure, psia
T_{t1}	=	stagnation temperature, °R
H_{t1}	=	stagnation enthalpy, BTU/lbm
P_{t2}	=	normal shock ratio of pressure, psia
α	=	angle of attack, deg.
β	=	angle of sideslip, deg.
δ_{LBF}	=	left body flap angle, deg.
δ_{RBF}	=	right body flap angle, deg.
δ_A	=	body flap aileron angle ($\delta_{LBF} - \delta_{RBF}$), deg.
Re_∞	=	freestream unit Reynolds number, ft^{-1}
$Re_{\infty,L}$	=	freestream Reynolds number based on reference length
h	=	surface heat transfer coefficient, lbm/ft^2sec
h_{F-R}	=	Fay-Riddel stagnation point heat transfer coefficient, lbm/ft^2sec
q	=	surface heat transfer, BTU/ft^2sec
q_{F-R}	=	Fay-Riddel stagnation point heat transfer, BTU/ft^2sec

* Aerospace Engineer, Aerosciences Branch, Member AIAA
¶ Aerospace Engineer, Aerothermodynamics Branch
§ Aerospace Engineer, Reacting Flow Environments Branch
‡ Director of Research, Thermosciences Institute, ELORET, Member AIAA

Introduction

A NASA Johnson Space Center team of engineers has been organized to design a crew return vehicle (X-38) for returning six International Space Station (ISS) crew members to Earth based on the X-23/X-24A lifting body configuration. Lifting body aerodynamics are extremely beneficial for this mission because their cross range capability ultimately leads to a shorter on-orbit loiter time. The X-23/X-24A configurations have flown (circa 1966-1971) during the United States Air Force sponsored sub-orbital hypersonic/supersonic flights of the X-23 (PRIME) program, and the transonic/runway landings of the X-24A (PILOT) program. The aerodynamic and aerothermodynamic information recovered from the X-23 and X-24A programs have served as the basis for preliminary trajectory and aerothermodynamic environment definitions (Ref. 1 - 2). However, because the X-38 design is a hybrid of these two configurations developed to fly hypersonically as well as subsonically, the aerodynamic and aerothermodynamic databases are being redeveloped with modern numerical and wind tunnel techniques.[3] Reference dimensions for the full scale vehicle and the wind tunnel model scales used for the hypersonic testing are provided in Table I.

Model	*Scale*	*Sref* [in^2]	*b* [in]	*L* [in]
X-38 Flight	1.0	23,328	120	276
Tunnel Series A	0.021	10.287	2.52	5.796
Tunnel Series B	0.036	30.570	4.34	9.991

Table I. X-38 Reference Dimensions

The scope of the aerothermodynamic tests was intended to provide a general understanding of the heating characteristics with respect to various geometric and aerodynamic parametrics including δ_{BF}, δ_A, surface roughness effects, α, β, Mach number, and Reynolds number. In the hypersonic flight regime, the X-38 is intended to fly at a nominal α of 40°, with an expected trim δ_{BF} between 20° and 25°. This α provides sufficient cross range capability to satisfy the ISS crew vehicle return mission and also provides enough aerodynamic drag to moderate the stagnation point heating. In order to provide a more limited scope for this paper, a baseline aerodynamic configuration with α at 40° and δ_{BF} at 25° will be discussed. The testing completed to date on the Revision 3.1 geometry includes a wide variation of the parametrics listed above. Publications detailing the entire set of experimental results are in revision[4] and will be published in the near future. The Revision 3.1 geometry, which is a hybrid X-23/X-24A, has served as the outer mold line reference for the X-38 program and is shown in the baseline hypersonic configuration in Fig. 1.

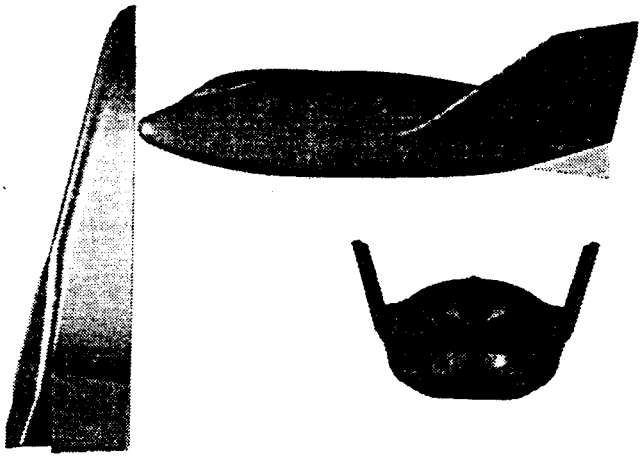

Figure 1. X-38 Geometry in the Baseline Hypersonic Aerodynamic Configuration

Experimental Methods

Facilities

Two conventional blow down hypersonic wind tunnels were used in this study. They are the NASA Langley Research Center (LaRC) 20-Inch Mach 6 Air Tunnel and the 31-Inch Mach 10 Air Tunnel. The major components of each are a high pressure bottlefield, settling chamber, nozzle, test section, diffuser, and vacuum spheres. The flow is heated by an electrical resistance heater in both facilities. An injection system is used which can insert models from a sheltered position to the tunnel centerline in approximately 0.5 seconds. Flow conditions are determined either from calibrations using stagnation values as inputs or from the ratio of a pitot probe pressure-stagnation pressure to obtain Mach number. Recent calibrations and more detailed descriptions of the facilities are found in Ref. 5 and 6.

Test Conditions: Nominal reservoir stagnation and corresponding freestream flow conditions for the Mach 6 and Mach 10 tunnels are presented in Tables II and III. Test-section flow conditions in the 20-Inch Mach 6 Air Tunnel were determined from the measured reservoir pressure and temperature and the measured pitot pressure at the test section. Flow conditions for the 31-Inch Mach 10 Air Tunnel were based on measured reservoir pressures and temperatures and a recent unpublished calibration of the facility.

Re_∞ ($x10^6$)	M_∞	P_{t1} (psi)	T_{t1} (°R)	H_{t1} (BTU/ lbm)	P_{t2} (psi)
1.16	5.88	60.33	880.1	211.7	1.95
1.60	5.9	85.45	885.7	213.1	2.71
1.87	5.92	101.7	894.8	215.3	3.19
2.24	5.94	125.2	906.3	218.1	3.88
2.51	5.95	140.7	905.8	218.0	4.33
2.76	5.95	155.5	906.3	218.5	4.76
3.2	5.96	181.1	906.2	218.1	5.5
3.73	5.97	211.9	906.7	218.3	6.4
4.42	5.98	252.2	907.2	218.4	7.57
5.52	6.00	329.7	929.5	223.9	9.81
6.71	6.01	402.2	928.6	223.7	11.86

Table II. Nominal Flow Conditions for the LaRC 20-Inch Mach 6 Tunnel.

Re_∞ ($x10^6$)	M_∞	P_{t1} (psi)	T_{t1} (°R)	H_{t1} (BTU/ lbm)	P_{t2} (psi)
0.6	9.68	347.3	1768	442.1	1.199
1.1	9.78	721.3	1821	457.3	2.357
2.2	9.93	1452.0	1820	458.1	4.506

Table III. Nominal Flow Conditions for the LaRC 31-Inch Mach 10 Tunnel

Test Techniques

Heating: The rapid advances in image processing technology which have occurred in recent years have made digital optical measurement techniques practical in the wind tunnel. One such optical acquisition method is two-color relative-intensity phosphor thermography, which is currently being applied to aerothermodynamic testing in the hypersonic wind tunnels of NASA LaRC (Refs. 7-9). With this technique, ceramic wind tunnel models are fabricated and coated with phosphors which fluoresce in two regions of the visible spectrum when illuminated with ultraviolet light. The fluorescence intensity is dependent upon the amount of incident ultraviolet light and the local surface temperature of the phosphors. A temperature calibration of the system conducted prior to the study provides the look-up tables which convert the ratio of the green and red intensity images to global temperature mappings. After injection of an illuminated phosphor model into the wind tunnel, color video camera fluorescence intensity images are acquired. Calibrations providing surface temperature from the fluorescence intensity images are then applied to calculate surface temperature mappings. Typically, the camera field of view is adjusted to include the entire model. However, if necessary the camera field of view can be adjusted to provide additional resolution for specific localized phenomena. With temperature images acquired at different times in a wind tunnel run, global heat transfer images are computed assuming one-dimensional semi-infinite slab heat conduction. The primary advantage of this technique is the global resolution of the quantitative heat transfer data. Such data can be used to identify the heating footprint of complex, three-dimensional flow phenomena (e.g., flow separations and reattachments, shock impingements, the onset of boundary layer transition, etc.) that are extremely difficult to resolve by discrete measurement techniques. Since comparisons of heat transfer measurements using conventional thin-film resistance gauges and phosphor thermography have shown excellent agreement,[8,10] phosphor thermography is now routinely used in NASA LaRC hypersonic facilities.

Heating Data Reduction and Uncertainty: To analyze the large amount of data associated with phosphor thermography, a workstation based image processing package called IHEAT has been developed by NASA LaRC. Written in a user-friendly windowing format, IHEAT consists of six programs to handle system calibrations along with data reduction, editing and viewing. Using IHEAT, data can be reduced to heat transfer images immediately after a run. An automated routine also provides plots of heating long the centerline and axial cuts. Heating rates were calculated with IHEAT from the global surface temperature measurements using one-dimensional semi-infinite slab heat-conduction equations, as discussed in detail in Refs. 9 and 10. Based on considerations presented in these two references, phosphor system measurement error is believed to be better than ±8 percent, with over all experimental uncertainty of ±15 percent. Wind tunnel heating distributions are presented in terms of the ratio of heat-transfer coefficients $h/h_{F\text{-}R}$, where $h_{F\text{-}R}$ corresponds to the stagnation-point heating to a 1-foot sphere scaled to the model size and was calculated based on the theory of Fay and Riddel. Repeatability for normalized centerline heat transfer measurements is generally found to be better than ±4 percent.

Flow Visualization: To assist in the interpretation of the surface heating images, flow visualization techniques in the form of schlieren and oil-flow capabilities were utilized. The 20-inch Mach 6 Air Tunnel is equipped with a pulsed white-light, Z-pattern, single-pass schlieren system with a field of view encompassing the entire 20-inch test core. Images were recorded on 70-mm film and digitally scanned for incorporation into this paper. The 31-Inch Mach 10 Air Tunnel does not currently have an operating schlieren system. Surface streamlines were obtained using the

oil-flow technique in both facilities. The ceramic model was spray-painted black to enhance contrast with the white pigmented oils used to trace the streamline movement. A thin basecoat of clear silicon oil was first applied to the surface, then a mist of medium sized pigmented-oil drops were sprayed onto the model surface. After preparation in this fashion, the model was injected into the airstream and the development of the surface streamlines were recorded with a conventional video camera. The model was retracted immediately following flow establishment and formation of the streamline patterns and post-run digital photographs were recorded with a Kodak high-resolution camera.

Models

In order to obtain accurate heat transfer data using the one-dimensional heat conduction equation, models need to be made of a material with low thermal diffusivity and well defined, uniform, isotropic thermal properties. Also, the models must be durable for repeated use in the wind tunnel and should deform minimally when thermally cycled. To meet these requirements, a unique, silica ceramic investment slip casting method has been developed and patented.[11] Utilizing this method, several ceramic 0.021 and 0.036 scale X-38 models were fabricated from molds created from resin patterns (see Table IV). These resin patterns are quickly (3-4 days) fabricated using rapid prototyping techniques. The final ceramic models are then coated with a mixture of phosphors suspended in a silica-based colloidal binder. This coating consisted of a 5:1 mixture of lanthanum oxysulfide (La2O2S) doped with trivalent europium and zinc cadmium sulfide (ZnCdS) doped with silver and nickel in a proprietary ratio. Between run refurbishment of the approximately 0.001-inch thick coatings is typically not required. The final step in the fabrication process is to apply fiducial marks along the body for accurate determination of spatial locations.

Model	Scale	Right Flap	Left Flap
A-1	0.021	0°	0°
A-2	0.021	25°	25°
A-3	0.021	20°	20°
B-1	0.0362	0°	0°
B-2	0.0362	20°	20°
B-3	0.0362	25°	25°
B-4	0.0362	30°	30°
B-5	0.0362	20°	25°
B-6	0.0362	0°	20°

Table IV. X-38 Slip Cast Ceramic Models

The effect of surface roughness on hypersonic boundary layer transition was also investigated. A method for simulating raised shuttle like tiles has been documented in Ref. 12. The same technique was used to simulate model surface roughness in Mach 6 testing on the X-38 configuration. Roughness elements were cut from 0.0025-inch thick Kapton tape and stacked as necessary to evaluate the effect of discrete roughness elements on the windward surface heating. They were located directly over fiducial marks placed on the model prior to testing in order to ensure a known location.

Computational Methods

Computational Fluid Dynamics Solutions

Codes: The numerical tools used for this study include two computational fluid dynamics code and an axisymmetric analog heating code. The flowfield solver, IEC3D[13-15], has been extensively validated for inviscid perfect gas and equilibrium air solutions based on the Shuttle Orbiter configuration. For inviscid solutions, IEC3D makes use of Van Leer's flux-vector splitting and the fluxes are extended to higher order using the upwind total variation-diminishing (TVD) scheme of Osher and Chakravarthy. The solutions are obtained using a finite volume multi-block scheme together with an LU-SGS (Lower-Upper Symmetric Gauss-Seidel) implicit solver. The axisymmetric analog streamline code, AA2LCH[16-18], is used for predicting the convective heating on hypersonic vehicles based on an inviscid flowfield solution. AA2LCH makes use of Eckert reference conditions and approximate laminar and turbulent boundary layer solutions to generate this information. The use of these two codes for predicting convective heating has been applied extensively to the Shuttle Orbiter at both wind tunnel and flight conditions. Additional information about the application of IEC3D and AA2LCH to the X-38 configuration can be found in Ref. 1.

The second computational fluid dynamics code used in this work is the General Aerodynamic Simulation Program (GASP v3.0).[19] The code solves the full Navier-Stokes equations including species equations for thermochemistry with a finite-volume spatial discretization. The transport properties are calculated with Wilke's mixing rule with curve fits for the viscosities given by Blottner, et. al., Eucken's relation for thermal conductivity, and binary diffusion with a constant Schmidt number of 0.8. The third-order Van Leer (via MUSCL) flux splitting scheme with the min-mod limiter is used to calculate the inviscid fluxes and a central-difference approximation is used for the viscous fluxes. The discretized system of equations can be solved in many different ways, such as using point-Jacobi, Gauss-Seidel, or two-factor ADI. Two-factor

ADI is used for the results herein. Additional information about the application of GASP to the X-38 configuration can be found in Ref. 20. For both methodologies, the two-layer technique or the Navier-Stokes solutions, a constant wall temperature of 540 °R and a fixed ratio of specific heats (γ) of 1.4 was used.

Convergence Criterion: Typical convergence criteria involve examining the evolution of the residuals in the flowfield. For a typical solution, both the L_2 and the L_∞ norms drop four orders of magnitude or more in 2500 iterations and both values are typically within an order of magnitude of each other. In addition, for the application of the inviscid flowfield solutions to convective heating analyses, a surface entropy criterion is included as a convergence determination. The solution is said to be fully converged when the windward centerline entropy decrement approaches 5% of the stagnation value.[1]

Geometry and Grids

The surface representation for computational solutions was created in the PRO ENGINEERING[21] solid modeling software and was transferred to the ICEMCFD[22] software package in order to construct an initial surface body grid. The ICEMCFD surface grid was then transferred to the GRIDGEN[23] structured grid generation package in order to refine the surface grid and add additional features such as the body flap deflection. The volume grids were generated hyperbolically using the HYPGEN[24] program. The vehicle aerodynamic surfaces were set to 25° for the lower flap and 10° outboard for the rudder, i.e. the baseline hypersonic configuration. The inviscid grids have 165 streamwise points, 60 body to outer boundary points, and 130 points in the circumferential direction at the finest grid level.

Discussion of Results

Experimental Observations

Flow Visualization Features: Characteristic of all supersonic/hypersonic flowfields, the flow is dominated by the effect of the shock structures inherent to the particular configuration of interest. For the purposes of this discussion, we will restrict our observations to the baseline hypersonic configuration. A schlieren image for a Mach 6 free stream for this baseline configuration is presented in Fig. 2. The main windward flowfield features visible in this image are the bow shock, the boundary layer separation induced shock wave emanating from the separation zone in front of the flaps, the flap generated shock wave, and a complex bow shock-flap shock interaction region downstream of the vehicle. On the leeward side, the Schlieren image reveals a weak shock emanating from the canopy. Note the lack of any compression wave emanating from the leading edge of the fin. Based on these results alone, there does not appear to be any fin leading edge heating issues associated with shock interactions on the fin.

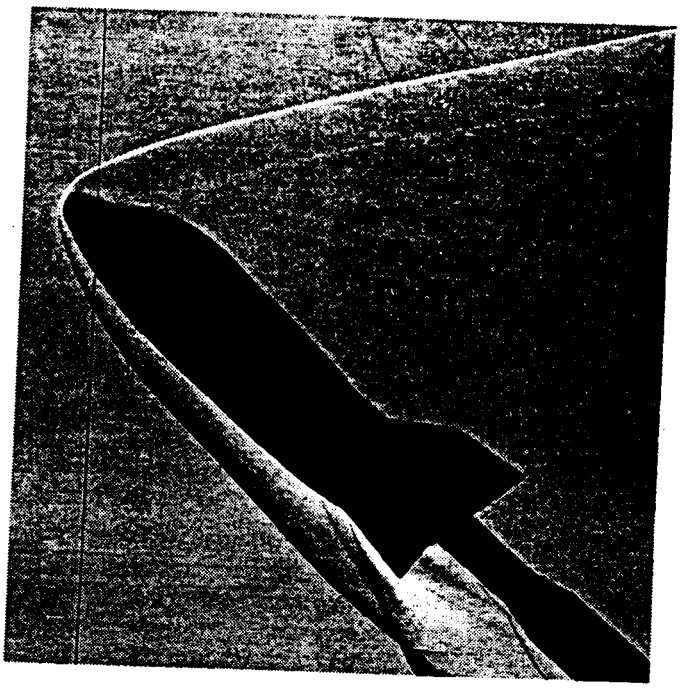

Figure 2. X-38 Baseline Configuration Mach 6 Schlieren Image.

By examining the corresponding surface oil flow pattern (Fig. 3), additional evidence to support these features can be found. In the nose region there appears to be a strong outward pressure gradient which expands the flow around to the leeward side. The windward side attachment line appears to remain on the windward surface and does not wrap around on to the side of the vehicle until the flap region is approached. The flow near the centerline of the vehicle can be characterized by mainly two dimensional flow with slight spreading of the oil flow patterns near the shoulder as the attachment line is approached. Outside of the attachment line, evidence of a strong outboard pressure gradient due to the expansion of the flow to the side of the vehicle is seen. Supporting what was seen in the schlieren image, a separated region is apparent near the hinge line of the flap which reattaches at about 30% of the flap chord. On the flap itself, there is moderate inflow near the centerline and a strong outboard flow pattern indicative of an expansion of the flow around the flap edge.

Figure 3. X-38 Baseline Configuration Mach 6 Air Oil Flow.

Heating Images: In addition to the combined results of the aforementioned schlieren and surface oil flow patterns, we can find further confirmation of these features by examining a surface heating image obtained at similar conditions for the baseline configuration at Mach 6 and 10 (see Fig. 4). The geometry aspect ratios of Figures 4a and 4b appear to be different. This perspective change is taken into account when comparing quantitative results. Specific flow condition information for each of the heating images in this section are provided in Table V.

Associated with the stagnation region there is a horseshoe shaped high heat flux region attributed to both the stagnation point heating and flow expanding onto the side of the vehicle. This flow expansion results in a decrease in boundary layer thickness and increased heating. Near the centerline of the vehicle the heating is fairly uniform, consistent with a mainly

Run / Model	M_∞	Re_∞ ($x10^6$)	P_{t1} (psi)	T_{t1} (°R)	H_{t1} (BTU/ lbm)
21/B-3	5.878	1.14	59.42	880.4	211.8
22/B-3	5.936	2.235	124.7	904.1	217.6
119/B-3	5.936	2.25	126.2	906.9	218.3
37/A-2	9.783	1.109	718.1	1820	457.0
38/B-3	9.789	1.137	718.2	1797	450.7

Table V. Specific Flow Conditions for the LaRC 20-Inch Mach 6 and LaRC 31-Inch Mach 10 Air Tunnels

two dimensional flow pattern. Due to the expansion of theflow outboard of the attachment line, there is increased heating near the shoulder. As evidenced by the surface oil flow, there is a region of low heating in the flap hinge line region due to a separated flow. As the separated region reattaches to the flap, the heating increases and remains quite uniform across the remainder of the flap. The same surface heating features are demonstrated in Fig. 4b for a Mach 10 freestream with the same orientation and aerodynamic configuration as Fig. 4a. In addition to these features, however, we see slightly increased heating levels on the outboard and inboard edges of the flaps.

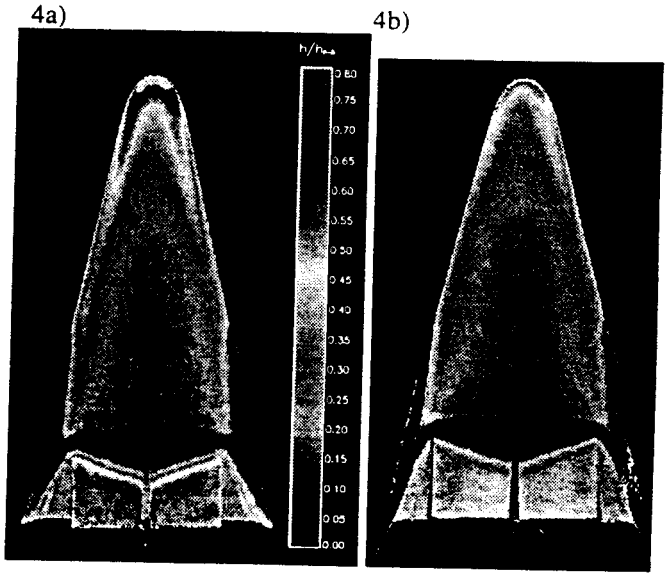

Figure 4. Global Heating Images for the X-38 Baseline Configuration
(a) Mach 6, $Re_\infty = 1.1x10^6$, Run 21, Model B-3.
(b) Mach 10, $Re_\infty = 1.1x10^6$, Run 38, Model B-3.

5a) 5b)

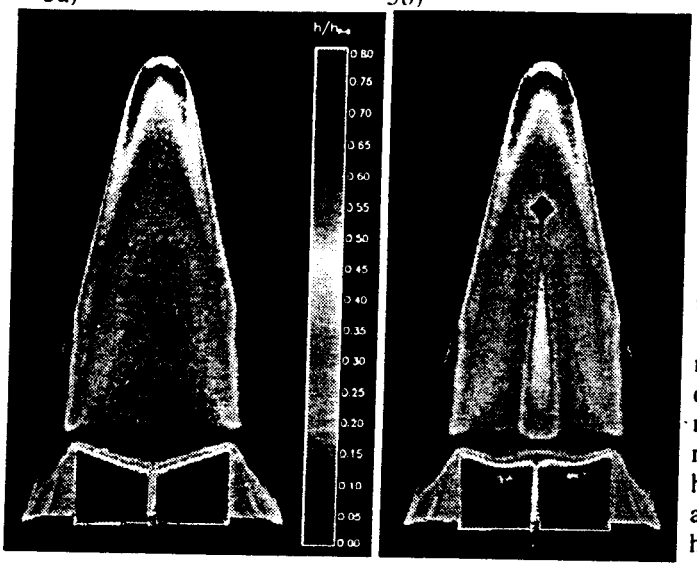

Figure 5. Global Heating Images for the X-38 Baseline Configuration
(a) Mach 6, $Re_\infty = 2.2x10^6$, Run 22, Model B-3.
(b) Mach 6, $Re_\infty = 2.2x10^6$, Run 119, Model B-3, 0.005-inch trip at X/L or 0.3

Reynolds Number and Boundary Layer Transition Effects: In order to evaluate the effect of Reynolds number and boundary layer transition effects on the windward surface heating, let us now discuss the same baseline configuration presented in the Shock Layer Features section, but with a factor of two larger Reynolds number. Figure 5a depicts the X-38 baseline hypersonic configuration in a Mach 6 freestream for this higher free stream Reynolds number. The same general flow features described in the previous paragraphs are also evident here. The only distinction between these images is the higher heating levels on the flaps. By placing a square roughness element on the centerline of the vehicle at X/L of 0.3, we are able to trip the boundary layer of the windward surface in a wedge shaped pattern downstream of the trip (see Figure 5b). The dimensions of the roughness element were selected to correspond approximately to the full scale vehicle's tile dimensions, and the 0.005-inch height was found to be nearly effective as a boundary layer trip. The relevant features of this transitional turbulent flow include a nominal heating region immediately downstream of the trip on the centerline with slightly elevated heating downstream of the roughness element corners corresponding to vortex action. The heating then increases about one to two trip lengths downstream and begins to spread at nearly a constant angle. The fact that the turbulent wedge spreads at a constant rate further supports the fact that the centerline of the vehicle has mainly two dimensional flow. In the separated region, slightly elevated heating is indicated within a region inboard of a projection of the turbulent wedge onto the flap reattachment. In the region of the boundary layer reattachment outboard of the turbulent wedge, we see heating levels at or above the reattachment heating of the untripped configuration. Downstream of the turbulent wedge, reattachment heating levels lower than the untripped configuration, but perhaps slightly higher than the lower Reynolds number results are evident.

The following table is a brief synopsis of the flap reattachment heating levels. The tripped flow column delineates whether a simulated tile was placed on the model to trip the flow as in Figure 5b. The reattachment heating levels listed correspond to the heating at the boundary layer reattachment on the flap, and the flap heating levels listed correspond to the heating downstream of the boundary layer reattachment. In the Reattach Heating column are two sets of data for the Mach 6, $2.2x10^6$ Re_∞ case which correspond to the heating levels outboard (OB) and inboard (IB) of the turbulent wedge.

M_∞	Re_∞	Tripped Flow	Reattach Heating (OB/IB)	Flap Heating
6	$1.1x10^6$	No	0.5 - 0.6	0.4 - 0.5
10	$1.1x10^6$	No	0.3 - 0.35	0.25 - 0.3
6	$2.2x10^6$	No	0.7 - 0.8	0.6 - 0.7
6	$2.2x10^6$	Yes	0.7 - 0.8 / 0.6 - 0.7	0.6 - 0.7

Table VI: Summary of Flap and Flap Reattachment Heating levels from the Mach 6 and 10 facilities for the Baseline Configuration.

For purposes of this discussion we will assume that the $1.1x10^6$ Re_∞ results are fully laminar on the flaps. Further investigation is needed to confirm this assumption. From Table VI we can make the following statements about the heating levels on the flaps if we make the laminar flap flow assumption. Laminar reattachment levels of heating would seem to be 10-20% higher than the laminar flap heating as seen in the $1.1x10^6$ Re_∞ runs at Mach 6 and 10. Transitional reattachment heating levels are 100-110% higher than the laminar flap heating levels, and turbulent reattachment heating levels are 25-40% higher than the laminar flap heating. Turbulent levels of heating on the flap downstream of the boundary layer reattachment are 50-60% higher than the laminar flap heating levels. These differences in heating levels seem to be consistent with a conclusion that the effects being demonstrated are the result of laminar, transitional, or turbulent flow on the flaps. The state of the

reattachment region appears to show evidence of being laminar, transitional or turbulent, and the flap heating downstream of the reattachment appears to be unable to sustain transitional heating levels. Hence, only laminar and turbulent levels of heating downstream of the boundary layer reattachment can be determined.

Quantitative Comparison of Experiment and Numerical Results

The heating images depicted in Figures 4-5 are the result of a global mapping technique which can provide both acreage and discrete information about surface heating on a configuration. By taking account for geometrical effects upon the viewing state of an imaging system, line cuts can be taken from these global images to present quantitative, discrete results for the surface heating distributions. Surface cuts from the baseline configuration at Mach 6 and 10, together with line cuts from CFD solutions at the Mach 10 condition are presented in Figures 6-9 for the centerline and a non-dimensional axial location of 0.5. Non-dimensionalization factors Lx and Ly were used in these figures for the X and Y coordinates respectively. The values of Lx and Ly used were 282.5 inches and 86.75 inches, respectively, both scaled to the appropriate model size. The wind tunnel data is presented as heat transfer coefficient non-dimensionalized by a Fay-Riddel stagnation point heat transfer coefficient (h/h_{F-R}) and upper and lower lines are included to illustrate the experimental uncertainty of ±15 percent. The CFD data is presented as heat transfer non-dimensionalized by a Fay-Riddel stagnation point heat transfer (q/q_{F-R}). In order to provide a comparison to the wind tunnel results, the CFD results are plotted together with the upper and lower experimental uncertainty bands in heat transfer coefficient form

Good agreement is seen between the two sets of wind tunnel data at Mach 6 and 10, demonstrating only slight differences with Mach number near the nose. Investigation of this difference has determined that this is due to a camera perspective effect on the 31-Inch Mach 10 data. The image data from the Mach 6 tunnel was acquired with the camera perpendicular to the model, while the initial Mach 10 data needs to be corrected for a 15° viewing angle. *(Inclusion of the corrected 31-Inch Mach 10 results into this paper was not possible due to time constraints for printing.)* Newly corrected data from the Mach 10 test agrees extremely well with the Mach 6 test results. Two sets numerical predictions are included in Figs. 7 and 9. One result is from the Navier-Stokes CFD described in detail in Ref. 20, and results from the two-layer technique described earlier are also included. Agreement within the experimental accuracy is illustrated for the Navier Stokes results, with the two-layer results tending to be low on the centerline.

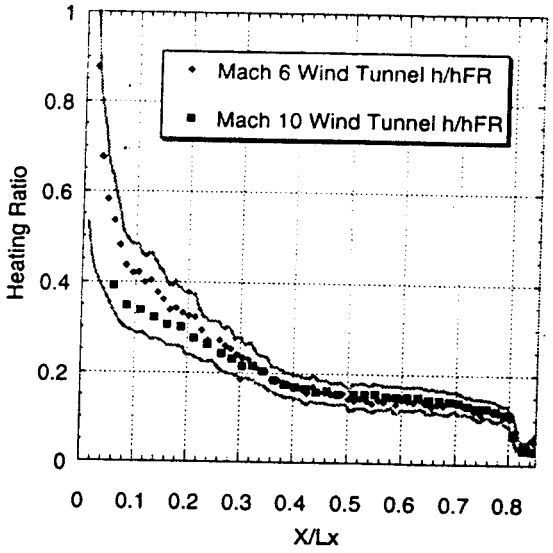

Figure 6. X-38 Baseline Configuration Centerline Heat Transfer Coefficient Ratio for Mach 6 (Run 21) and Mach 10 (Run 38) Tunnels at Re_∞ of $1.1x10^6$ with Model B-3.

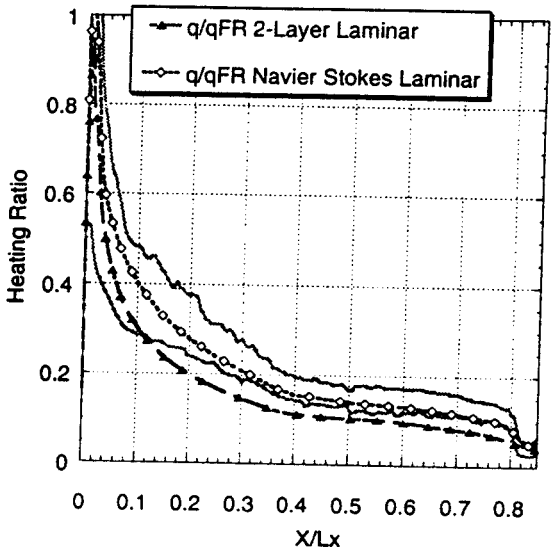

Figure 7. X-38 Baseline Configuration Centerline CFD Heat Transfer Ratio Comparison for Mach 10 Tunnel Conditions at Re_∞ of $1.1x10^6$.

Past an X/L_x of 0.8, both sets of centerline CFD results fail to capture the beginning of the boundary layer separation accurately. A two-layer method will not provide accurate results in this situation, and the

grid for the Navier-Stokes results was not optimized for resolutions of the separated region.

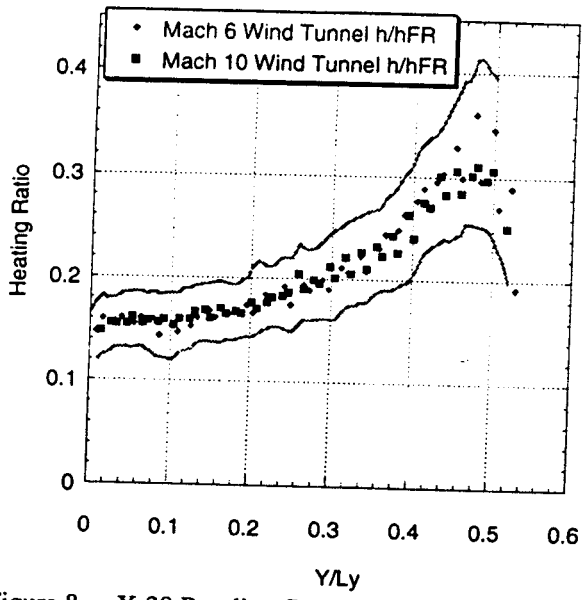

Figure 8. X-38 Baseline Configuration X/L of 0.5 CFD Heat Transfer Ratio Comparison for Mach 10 Tunnel Conditions at Re_∞ of $1.1x10^6$.

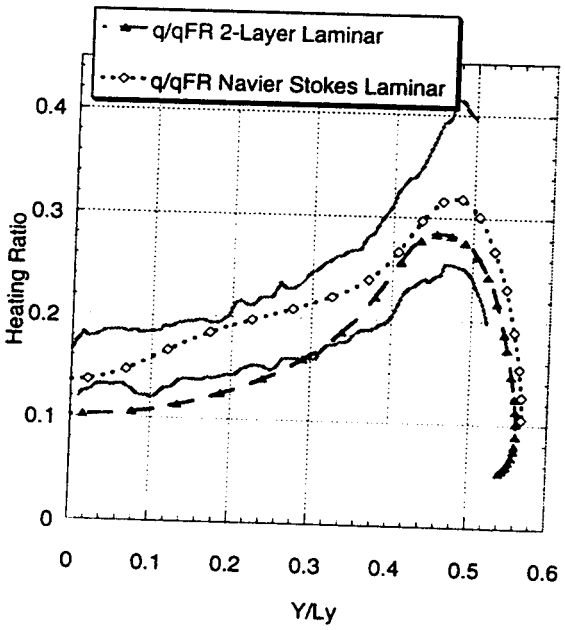

Figure 9. X-38 Baseline Configuration X/L of 0.5 CFD Heat Transfer Ratio Comparison for Mach 10 Tunnel Conditions at Re_∞ of $1.1x10^6$.

The accuracy of the CFD results included herein are acceptable for acreage thermal protection system design for the X-38. Current X-38 acreage thermal protection system material selection is not being driven beyond current material technologies.[1] Specific local thermal protection system design issues will incorporate sufficient margins to encompass uncertainties of the magnitude presented in these comparisons.

Conclusions

Aerothermodynamic wind tunnel testing in support of the X-38 crew return vehicle design has been conducted at NASA Langley Research Center Mach 6 and 10 hypersonic facilities. Together with schlieren images and surface oil flows, a more complete understanding of the windward surface flow features and heating patterns has been presented. The major features of the windward surface flowfield include mainly two dimensional flow near the centerline and a separation region near the flap hinge line. An expansion of the flow onto the shoulder of the vehicle results in increased heating, and the reattachment of the separated flow at the flap hinge line results in laminar, transitional or turbulent heating levels on the body flaps. The experimental heating results indicate that transitional reattachment heating on the flaps can have significant impact on flap heating levels. Comparisons of line cuts taken from the thermal phosphor imaging technique with two-layer and Navier Stokes computational fluid dynamics surface heating results are within acceptable uncertainties for the design of the X-38.

Acknowledgements

Support provided to the seventh author through Contract NAS2-14031 from the NASA ARC Reacting Flow Environments Branch, and assistance provided by Carol B. Davies of Sterling Software for reducing computational fluid dynamics results for comparison to the experimental data is gratefully acknowledged.

References

1. Campbell, C.H., Caram, J., Li, C.P., and Madden, C., "Aerothermodynamic Environment Definition for an X-23/X-24A Derived Crew Return Vehicle," 31st Thermophysics Conference, June, 1996, AIAA 96-1862.

2. Campbell, C.H., Joosten, B.K., and Meyerson, R.E., "Johnson Space Center Crew Return Vehicle Activities," SPACE 96 - Fifth ASCE International Conference on Engineering, Construction and Operations in Space, June, 1996.

3. Campbell, C., Caram, J., Berry, S., DiFulvio, M. and Horvath, T., "Overview of X-38 Hypersonic Wind Tunnel Data and Comparison with Numerical Results," 35th Aerospace Sciences Meeting and Exhibit, January, 1997, AIAA 97-0567.

4. Berry, S.A., Horvath, T.J., Robach, V.E., and Williams, G.B. Jr., "Results of the .0362-Scale X-38 (Rev. 3.1) Vehicle Aerothermodynamic and Boundary Layer Transition Test in the NASA Langley 20-Inch Mach 6 Tunnel," NASA TM 112857, 1997.

5. Micol, J.R., "Hypersonic Aerodynamic/Aerothermodynamic Testing Capabilities at Langley Research Center: Aerothermodynamic Facilities Complex," 30th Thermophysics Conference, San Diego, CA, June 19-22, 1995, AIAA 95-2107.

6. Miller, C.G., "Langley Hypersonic Aerodynamic/Aerothermodynamic Testing Capabilities - Present and Future," 16th Aerodynamic Ground Testing Conference, June 18-20, 1995, Seattle, WA, AIAA 90-1376.

7. Buck, G.M., "Surface Temperature/Heat Transfer Measurement Using A Quantitative Phosphor Thermography System," 29th Aerospace Sciences Meeting, Reno, NV, January 7-10, 1991, AIAA 91-0064.

8. Merski, N.R., "A Relative-Intensity Two-Color Phosphor Thermography System," NASA TM 104123, September, 1991.

9. Merski, N.R., "An Improved Two-Color Relative-Intensity Phosphor Thermography Method for Hypersonic Wind Tunnel Aeroheating Measurements," Ph.D. Dissertation, George Washington University, 1997.

10. Micol, J.R., "Aerothermodynamic Measurement and Prediction for a Modified Orbiter at Mach 6 and 10 in Air," 26th Thermophysics Conference, Honolulu, HI, June 24-26, 1991, AIAA 91-1436.

11. Buck, G.M. and Vasquez, P., "An Investment Ceramic Slip-Casting Technique for Net-Form, Precision, Detailed Casting of Ceramic Models," U.S. Patent 5,266,252, November 30, 1993.

12. Berry, S.A., Bouslog, S.A. Brauckmann, G.J., and Caram J.M., "Boundary Layer Transition Due to Isolated Roughness: Shuttle Results from the LaRC 20-Inch Mach 6 Tunnel", 35th Aerospace Sciences Meeting and Exhibit, January, 1997, AIAA 97-0273.

13. DeVenezia, J., Wang, K.C., and Caram, J.M., "Space Shuttle Orbiter Wing Leading Edge Heating Predictions and Measurements," Orbiter Experiments Aerothermodynamics Symposium, April, 1995.

14. Tam, L.T., "LU-SGS Implicit Scheme for Entry Vehicle Flow Computation and Comparison with Aerodynamic Data," AIAA-92-2671-CP, June 1992.

15. An, M.Y., Wang, K.C. and Tam, L.T., "Computation of Inviscid Flowfield Around 3-D Aerospace Vehicles and Comparison with Experimental and Flight Data," AIAA-93-0885, January, 1993.

16. Cooke, J.C., "An Axially Symmetric Analogue for General Three-Dimensional Boundary Layers," British A.R.C., R&M No. 3200, 1959.

17. DeJarnette, F.R., and Davis, R.M., "A Simplified Method for Calculating Laminar Heat Transfer Over Bodies at an Angle of Attack," NASA TN D-4720, 1968.

18. Wang, K.C., "An Axisymmetric Analog Two-Layer Convective Heating Procedure with Application to the Evaluation of Space Shuttle Orbiter Wing Leading Edge and Windward Surface Heating," NASA CR-188343, Oct., 1993.

19. "GASP v3.0 User's Manual," Aerosoft Inc. 1996.

20. Loomis, M.P., Venkatapathy, E., Davies, C.B., Campbell, C.H., Berry, S.A., Horvath, T.J., and Merski, N.R., "Aerothermal CFD Validation and Prediction for the X-38 Program," 32nd Thermophysics Conference, Atlanta, GA, June 23-25, 1997, AIAA 97-2484.

21. ProEngineer, a product of Parametric Technology Corporation.

22. ICEMCFD/CAE MULCAD, version 3.1.3.0 Reference Manual, July, 1994.

23. Chawner, J.R., and Steinbrenner, J.P., "GRIDGEN Version 10 Training Course Notes," 1994.

24. Chan, W.M., Chiu, I.T., Buning, P.G., "User's Manual for the HYPGEN Hyperbolic Grid Generator", September, 1993.